Article

Optical Power Conversion via Tunneling of Plasmonic Hot Carriers

Shengxiang Wu[†] and Matthew T. Sheldon[*,†,‡]

[†]Department of Chemistry and [‡]Department of Material Science & Engineering, Texas A&M University, College Station, Texas 77843-3255, United States

ABSTRACT: Optical and photochemical power converters based on resonant absorption in metal nanostructures generally employ a mechanism whereby optically excited "hot" carriers are injected over a Schottky barrier at a semiconductor or molecular interface. This process is inefficient because most of the excited carriers relax and thermalize with the lattice before they can be collected. Here we outline an alternative strategy that can take better advantage of both optically excited and thermalized electrical carriers by leveraging the tunneling transport phenomenon across metal junctions that concentrate and absorb light preferentially on one side of a nanoscale gap. We have developed a general description for electron transport within a parabolic conduction band approximation accounting for both thermal (Fermi−Dirac) and nonthermal contributions to the steady-state electronic energy distribution that results from optical excitation. A nonzero current density is predicted when the excited-state distribution of carriers is dissimilar on opposite sides of a tunnel junction, with electrons emitted from the electrode that absorbs more light. An increase of the short-circuit photocurrent and the associated open-circuit voltage at elevated temperatures indicates a cooperative interaction between thermal and nonthermal excitation mechanisms. We also use full wave optical simulations (FDTD method) to demonstrate a simple device design for obtaining optical power conversion efficiency that is competitive with conventional photovoltaic devices.

KEYWORDS: hot carriers, plasmons, tunneling, photothermal, thermionic emission, photoemission
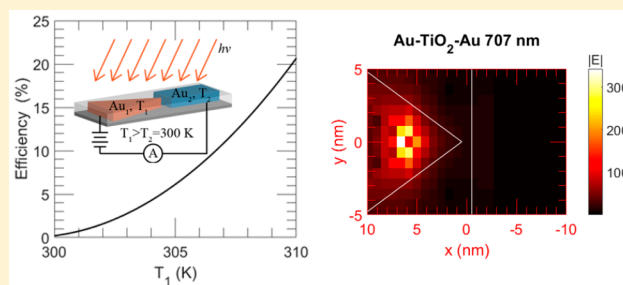
There has been significant recent research activity studying the use of plasmonic metal nanostructures for enhancing solar energy conversion in photovoltaic and photocatalytic devices.[1,2] The potential benefits provided by plasmonic nanostructures are due to the strong subwavelength optical field concentration that results from the coupling of resonant oscillations of free electrons in the metal, termed plasmons, with the incident light field. Because the frequency response and spatial distribution of the concentrated field depend on size and shape, plasmonic nanostructures can be tailored to optimize optical performance when integrated within photovoltaic (PV) and photocatalytic devices.[3] For example, plasmonic nanostructures have been widely studied to improve broadband absorption in the active layer of organic solar cells (OSCs), usually by placing the nanostructures at the surface of cells or embedded in the absorber layer.[4−6] Despite increasing absorption in the active layer, the field enhancement can also promote significant optical absorption in the metal that does not contribute to the device power conversion efficiency.[5,7] Therefore, direct absorption in the metal must be weighed against potential absorption enhancements in the active layer.

Alternatively, there has been significant interest in optical power conversion schemes that can take advantage of the resonant absorption in the metal.[8−12] After optical excitation a plasmon decays via Landau damping to generate electron−hole pairs. These "hot carriers" move ballistically through the metal with a mean-free path of approximately 10−100 nm until they relax and recombine, first via electron−electron scattering after

∼100 fs, followed by electron−phonon thermalization after ∼1 ps.[13−15] It has been demonstrated that these highly excited, nonthermal hot carriers can be injected over a Schottky barrier before relaxation, to be used for electrical or chemical work.[16−18] However, the hot carriers still require sufficient energy to overcome the interface barrier in order to escape the metal, in addition to momentum-matching requirements.[19] These constraints significantly impede the efficiency of carrier collection and power conversion, especially in the low-energy infrared (IR) spectral range.[20] In addition, only carriers generated within the mean-free path length of the interface can participate in charge transfer, with the remainder of the absorbed optical energy otherwise lost in the form of significant heating of the lattice.[21] Consequently, the optical power conversion efficiency record for a device based on hot carrier collection is currently 0.03%,[22,23] with a theoretical efficiency maximum of 1.4% identified for 4 eV incident photons.[19]

In this study we show how it is possible to more fully utilize the electrical carriers excited in a metal during optical absorption by taking advantage of tunneling transport phenomena to collect those carriers that have insufficient energy to overcome an interface barrier. Due to the optical tailorability of plasmonic nanostructures, it is straightforward to design tunneling junction geometries with a strong asymmetry in the optical response on opposite sides of a junction. This
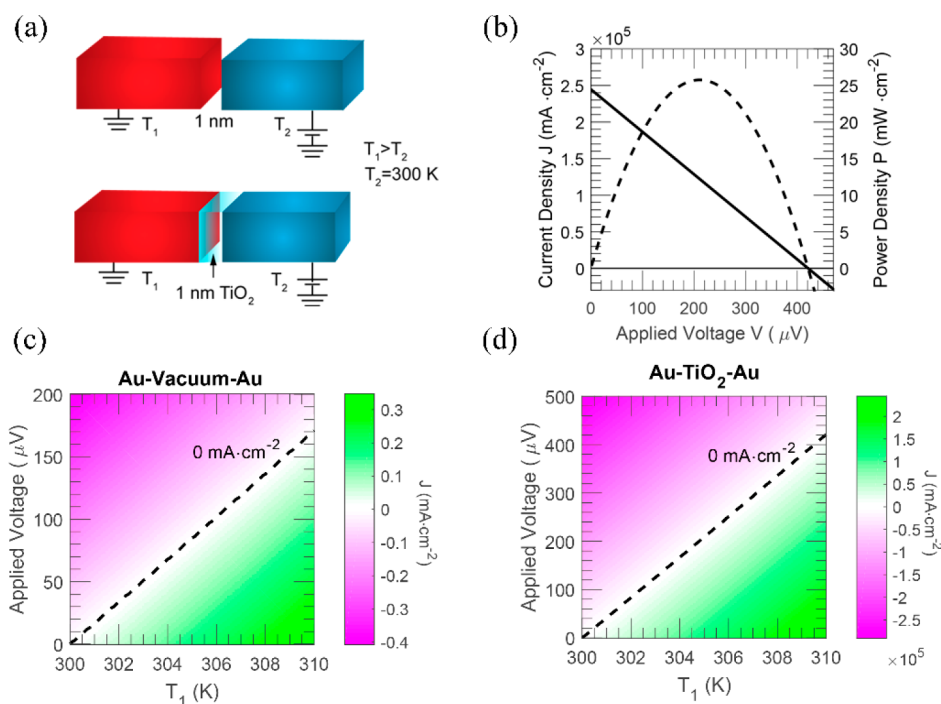
Figure 1. (a) Scheme of a Au−vacuum−Au (top) and a Au−TiO$_2$−Au (bottom) 1 nm gap tunnel junction subject to a thermal gradient, $\Delta T = T_1 - T_2$. (b) $J−V$ (solid) and $P−V$ (dashed) curve of the Au−TiO$_2$−Au junction when $T_1 = 310$ K and $T_2 = 300$ K. $J−V$ map as a function of T_1 and applied voltage with fixed $T_2 = 300$ K for (c) a Au−vacuum−Au junction and (d) a Au−TiO$_2$−Au junction. The dashed trace shows the open-circuit voltage at a given T_1.

asymmetry can promote optical absorption that results in both uneven photothermal heating and unbalanced optically excited electron distributions on opposite sides of a nanoscale gap. We show how any asymmetries in electronic structure across the gap will provide a tunneling current that can be used to provide electrical work. In our study elevated temperatures due to electron−phonon scattering and hot carrier distributions are analyzed within a consistent semiclassical framework.[24] Modified Fowler−Nordheim theory is used to analyze electron tunneling and thermionic emission. We also performed full wave optical simulations (FDTD method)[25] to model tunnel junction geometries with asymmetric optical absorption profiles and corresponding local electric field enhancement. Our results outline a strategy for optical power conversion efficiency exceeding 20% in simulations of practical device geometries under solar flux, with theoretical efficiencies of ideal geometries that significantly outperform other proposed strategies to date for optical power conversion via plasmonic absorption.

■ **METHODS**

Electron Transport across Plasmonic Tunneling Junctions. Under the conditions of resonant absorption and photothermalization considered in this study, electron tunneling, thermionic emission, and direct photoemission of hot electrons may take place across a plasmonic metal junction, as depicted in Figure 1a. A theoretical description of field emission from metal surfaces was first developed by Fowler and Nordheim, who approximated the electronic structure of the metal with a parabolic conduction band model.[26] Following the Fowler−Nordheim method, many subsequent studies have analyzed tunneling as well as thermionic emission and photoemission from metal surfaces or nanojunctions.[27,28] The electron distribution in the metal is calculated as

$$n(v)\,dv_x\,dv_y\,dv_z = \frac{2m^3}{h^3}f(E)\,dv_x\,dv_y\,dv_z \tag{1}$$

Here, n is the electron density, v is electron velocity, v_x, v_y, v_z are electron velocity in the x, y, z directions, respectively, m is electron mass, h is Planck's constant, and $f(E)$ is the Fermi−Dirac distribution function at energy E.

For simplicity, we consider electron transport in the x direction in order to rewrite eq 1 in terms of v_x.

$$n(v_x) = \frac{2m^3}{h^3}\iint_{-\infty}^{\infty}f(E)\,dv_y\,dv_z = \frac{2\pi m^2}{h^3}\int_0^{\infty}f(E)\,dE_r \tag{2}$$

where $v_r^2 = v_y^2 + v_z^2$, $E_x = \frac{1}{2}mv_x^2$, and $E_r = E - E_x = \frac{mv_r^2}{2}$.

The electron flux, N_{l-r}, from left to right, can be calculated by integrating the product of eq 2 with the electron velocity v_x and emission probability $D(E_x)$ for all possible electron energies.

$$N_{l-r} = \int_0^{\infty}v_x n(v_x)\,D(E_x)\,dv_x = \frac{1}{m}\int_0^{\infty}n(v_x)\,D(E_x)\,dE_x \tag{3}$$

The energy range of the integration in eq 3 accounts for three different electron transport mechanisms: tunneling, thermionic emission, and photoemission. Tunneling will occur with a probability defined by the transmission coefficient when the energy E_x is less than the junction barrier height, U.

$$D(E_x) = e^{-(2/\hbar)s\sqrt{2m(U-E_x)}} \tag{4}$$

Here, s is the size of the tunneling gap. Alternatively, thermionic emission and photoemission occur with unity efficiency, $D(E_x) = 1$, when electrons have sufficient thermal energy or energy from absorbed photons, respectively, to overcome the barrier height. In this study, we analyzed an Au−

vacuum−Au junction, where the barrier height $U = 4.6$ eV corresponds to the work function of gold.[21] We also considered an Au−TiO$_2$−Au junction with $U = 1$ eV based on the interfacial metal−semiconductor Schottky barrier height.[29]

Since electrons can be transmitted across the plasmonic junction from left to right and vice versa, the net current density J needs to account for electron transport in both directions.

$$J = e(N_{l-r} - N_{r-l})/S \qquad (5)$$

Here, e is unit charge of electron, S is the active area of the junction interface, and we have defined positive current to flow from left to right. Equation 5 indicates that if the plasmonic junction has identical electron distributions on both sides, the electron flux transmitted from left to right would cancel out the electron flux transmitted from right to left, resulting in zero net current density.

We consider how plasmonic absorption in the metal can break the symmetry of the junction in order to promote a net current density. We analyze electron transport that results from temperature differences across the junction due to uneven photothermalization and, separately, uneven hot carrier generation via differences in photoexcitation on opposite sides of the junction. Both of these effects can redistribute electron density $n(v_x)$ asymmetrically across the junction, thus resulting in a net current density. A temperature variation results in a different Fermi−Dirac distribution for electrons on either side of the junction. The hot side of the junction has more electrons occupying higher energy states and thus has greater probability for tunneling, even if the thermal energy is too small to provide a significant current due to thermionic emission. Photoabsorption directly excites nonthermal hot electrons into higher energy states that can either tunnel or overcome the energy barrier.

Hot Carrier Generation in Metallic Nanostructures. To determine the hot electron generation from photoabsorption and the corresponding excited-state distribution, we use the theoretical framework previously developed by Govorov et al.[21] and Manjavacas et al.[30] For simplicity, we first consider that one side of the plasmonic junction is a gold nanocube (inset, Figure 2a). Upon illuminating this nanocube with monochromatic x-polarized light, the electric field inside the gold nanocube $E_x(\omega)$ is approximately constant and is linearly related to the incident field strength within the quasistatic approximation, i.e., if the nanocube is small compared to the incident wavelength.[5] This induced electric field perturbs the free electrons in the metal,

Figure 2. Hot electron generation rate under 532 nm monochromatic irradiation at a power density of 1000 W/m^2 compared with the thermal distribution of electrons in a 5 nm Au cube at 300 K.

resulting in a nonequilibrium (hot carrier) distribution that can be calculated through a many-body density matrix.[21,30] The change in population $\mathbb{N}(\varepsilon_f, \omega)$ of a state with energy ε_f arising from the interaction with the incident photons of energy ω is treated as a perturbation and is calculated as[21,30]

$$\mathbb{N}(\varepsilon_f, \omega) = \frac{4}{\tau} \sum_i \sum_f (f(\varepsilon_i) - f(\varepsilon_f)) |\chi_{i,f}|^2$$

$$\left[\frac{1}{(\hbar\omega - \varepsilon_f + \varepsilon_i)^2 + \Gamma^2} \right.$$

$$\left. + \frac{1}{(\hbar\omega + \varepsilon_f - \varepsilon_i)^2 + \Gamma^2} \right] \delta(\varepsilon - \varepsilon_f) \qquad (6)$$

Here, f is the equilibrium Fermi−Dirac distribution function, Γ represents energy broadening. For gold nanostructures the energy broadening is 0.078 eV, corresponding to the relaxation energy of electron−phonon scattering.[21] τ is the electron relaxation time that accounts for both electron−electron and electron−phonon scattering. For electrons in gold nanostructures we use $\tau = 0.5$ ps, as determined by transient absorption experiments.[31] The matrix element $\chi_{i,f} = i\langle\phi|f\rangle$, where $\phi = xE_x$ is the potential induced by incident light inside the gold nanocube, and the subscripts, i and f, stand for the initial and final states in the calculation, respectively.

Full Wave Optical Simulations. In addition to the above quasistatic approximation, we also used full wave optical simulations (FDTD method, Lumerical Inc.)[25] to calculate the absorption and electric field distributions in more realistic device geometries that are optimized by designing asymmetries into the optical response across a nanoscale gap (Figure 4). In these studies, the modeled plasmonic tunnel junction consisted of a 20 nm thick smooth SiO$_2$ substrate on a Si wafer. On top of the SiO$_2$ layer, two 20 nm thick gold nanoelectrodes were placed with dimensions depicted in Figure 4a in order to define a tunnel junction. The Johnson and Christy dielectric function was used for gold, and a default dielectric function from the Lumerical database was used for SiO$_2$. Studies were also performed on this geometry coated with a 30 nm layer of TiO$_2$. The dielectric function of TiO$_2$ was adopted from Bodurov et al.[32] A mesh of 1 nm was used across the entire geometry, while a smaller mesh of 0.1 nm was used to resolve the features of the nanoscale gap region (2 nm × 2 nm × 10 nm) in the center of the simulation geometry.

■ RESULTS AND DISCUSSION

Optical absorption is a local quantity that can be calculated by integrating the product of frequency ω, the electric field strength $|E|^2$, and the imaginary part of the dielectric permittivity over the full volume of the nanostructure. During steady-state illumination uneven optical absorption on opposite sides of the plasmonic tunneling junction can be promoted by tailoring the optical response of each metallic nanoelectrode. This uneven absorption can provide a temperature gradient across the junction affecting all electrons, as well as a steady-state subpopulation of photoexcited electrons, which are in the process of thermalizing via electron−electron and electron−phonon scattering. Although both effects correspond to different stages of the same microscopic relaxation process, for simplicity we first analyze the transport behavior of the thermally distributed electrons separately from the transport
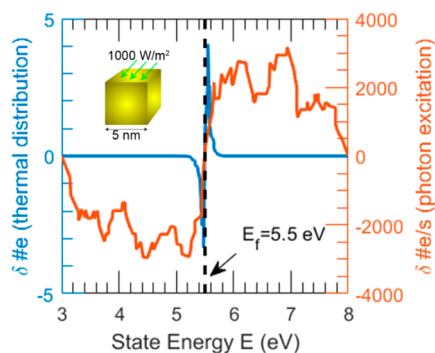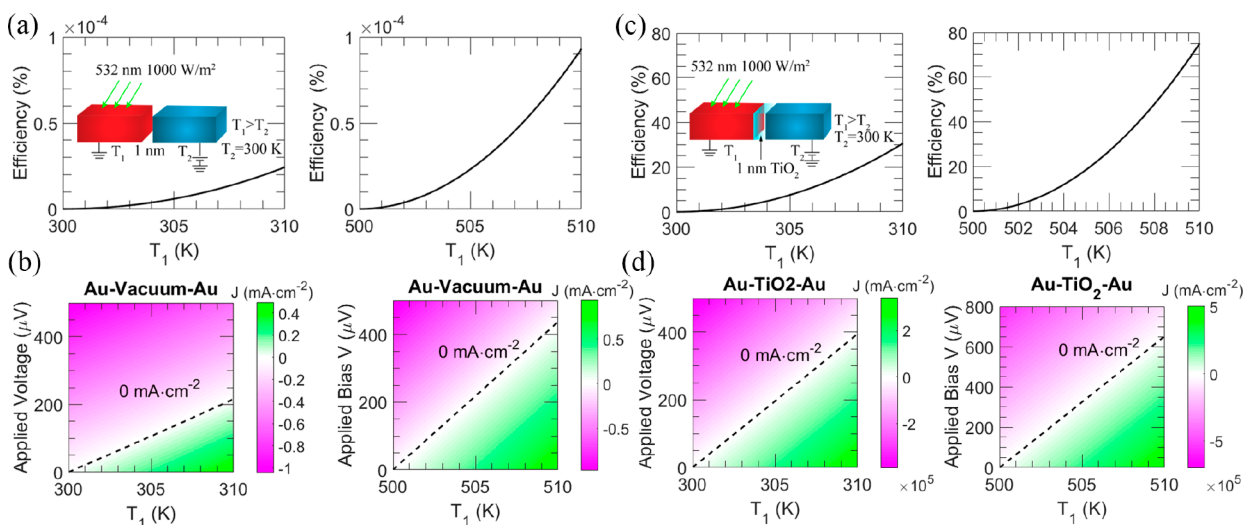
Figure 3. (a) Estimated optical power conversion efficiency of a Au−vacuum−Au junction and (b) the corresponding J−V map as a function of T_1 and applied voltage (left) with fixed $T_2 = 300$ K and (right) with fixed $T_2 = 500$ K. (c) Au−TiO$_2$−Au junction and (d) the corresponding J−V map as a function of T_1 and applied voltage (left) with $T_2 = 300$ K and (right) with $T_2 = 300$ K. All calculations considered a 5 nm Au cube and 532 nm monochromatic light with a power density of 1000 W/m^2.

behavior of photoexcited electrons. Both consequences of optical absorption can significantly modify the electron distribution on one side of the junction compared to the other, and both thermal and nonthermal electrons are expected to contribute to the net electrical current across an illuminated tunnel junction.

Once a thermal gradient is established, electrons that are not photoexcited are distributed in energy based on the Fermi−Dirac function and the local temperature. More electrons occupy higher energy states on the hot side of the junction and thus have greater tunneling probability. Figure 1 shows a summary of the transport calculations of plasmonic junctions with 1 nm tunneling gap subject only to a temperature gradient. Our calculation probed temperature differences that were varied between 0 and 10 K, which is consistent with temperature differences that were experimentally maintained in similar nanoscale thermophotovoltaic power generator devices.[33,34] A nonzero short-circuit current density, J_{SC}, is observed that flows from the hot to the cold nanoelectrode. In addition, a voltage V was calculated that was applied opposite the current direction, corresponding to a circuit load. The power density P provided by the junction is determined by the product of the applied voltage and the current density. The maximum applied voltage that completely canceled the tunneling current corresponds to the open-circuit voltage, V_{OC}, of the illuminated junction. In addition to modeling a Au−vacuum−Au junction, we also calculated the transport behavior of a Au−TiO$_2$−Au junction. Titanium dioxide (TiO$_2$) is a thermally stable, transparent, wide band gap insulator that is commonly used as an electrode for plasmonic hot electron-based devices, because fast electron injection over the interface Schottky barrier and good carrier collection are reported when TiO$_2$ is contacted to plasmonic metals.[35,36]

Figure 1c shows the current−voltage (J−V) characteristics of both modeled plasmonic junctions in a temperature range near 300 K. The short-circuit current density increases with larger temperature difference across the junction. More electrons are thermally activated on the hot side into states that have a higher probability of tunneling, so there is a net tunneling current. A current density up to 350 μA/cm^2 and an open-circuit voltage

of 170 μV for a maximum power density of 0.015 μW/cm^2 is predicted for the Au−vacuum−Au tunneling junction. It should be noted that this power density is solely attributed to electron tunneling, since there is negligible thermionic emission in this temperature range. The open-circuit voltage is comparable to the thermoelectric potential of Au based on the Seebeck coefficient of Au of 6.5 μV/K.[37] Although similar in design, the power density provided by this tunneling junction is smaller than typical thermionic emission devices.[38] However, the calculated current density is orders of magnitude larger than comparable thermionic devices operating at such a low temperature range. Typical thermionic devices are operated at much higher temperatures above 1000 K, and the emitting metal surface is usually treated with cesium vapor to decrease the work function barrier height to about 1 eV.[38] Since the tunneling probability is also limited by the dependence on the barrier height, i.e., the work function of Au in eq 4, we also compared these results with a shallower tunnel barrier of 1 eV, defined by the Au−TiO$_2$ Schottky barrier height (Figure 1b,d). A significant enhancement of short-circuit current to 2.446 × 10^5 mA/cm^2 is calculated, as well as an increase of the open-circuit voltage to 420 μV with a power density of 25 mW/cm^2 at the maximum temperature gradient ($\Delta T = 10$ K), as depicted in Figure 1b. Even for the Au−TiO$_2$−Au tunneling junction, such a high current density and power output are solely attributed to electron tunneling, because there is negligible thermionic emission at this temperature.

Upon illumination, direct photoexcitation of a subpopulation of electrons occurs, in addition to the photothermal heating of all electrons analyzed above. The calculated rate of nonthermal hot electron state occupation from photoexcitation in comparison with the Fermi−Dirac distribution of the unperturbed electron gas is depicted in Figure 2. The calculation is for a 5 nm gold nanocube at 300 K illuminated with 532 nm (2.33 eV) monochromatic illumination at a power density of 1000 W/m^2, comparable to solar flux. Due to electron−electron and electron−phonon scattering in combination with quantum confinement effects, hot electrons generated in small gold nanostructures tend to display a wider energy distribution than photoexcited bulk metals, with a
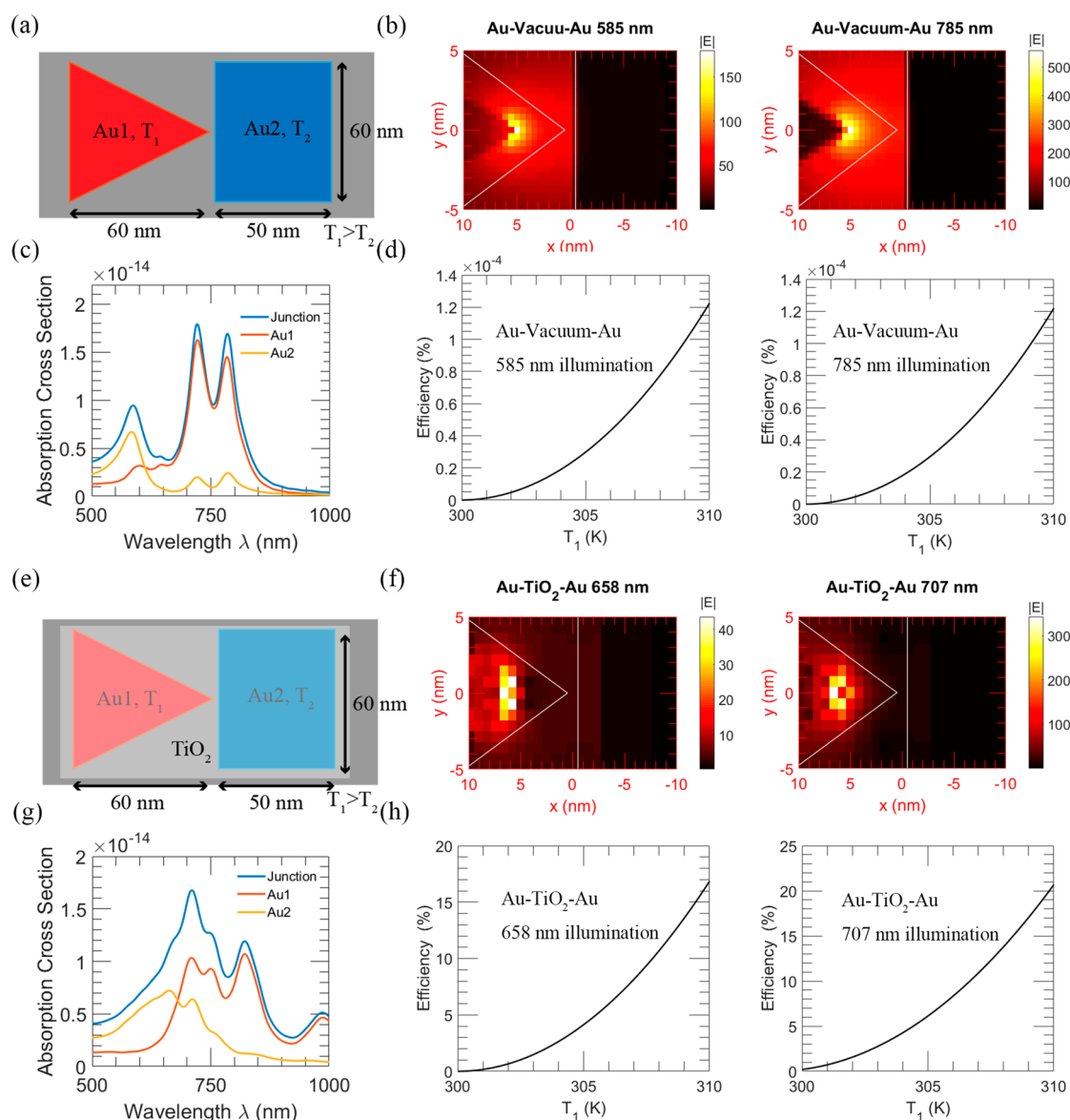
Figure 4. (a) Top-down schematic view of a Au−vacuum−Au device and (b) the corresponding electric field enhancement map of the 20 nm × 10 nm junction region for illumination at 585 nm (left) and 785 nm (right). (c) Calculated absorption spectrum (blue) of the device in (a) with the spatially integrated absorption by electrode Au1 (red) and electrode Au2 (yellow). (d) Estimated conversion efficiency for 585 nm illumination (left) and 785 nm illumination (right). (e) Top-down schematic view of a Au−TiO$_2$−Au device and (f) the corresponding electric field enhancement map of the 20 nm × 10 nm junction region for illumination at 658 nm (left) and 707 nm (right). (g) Calculated absorption spectrum (blue) of the device in (e) with the spatially integrated absorption by electrode Au1 (red) and electrode Au2 (yellow). (h) Estimated conversion efficiency for 658 nm illumination (left) and 707 nm illumination (right). All calculations are for an optical power density of 1000 W/m^2.

significant population of electrons across the range $E_f \pm h\nu$.[39] We expect that this large hot carrier energy distribution can facilitate a more energetic imbalance in the electron population in one nanoelectrode compared to the other, resulting in larger current densities compared with pure thermal gradients.

To quantify how hot electron generation can enhance unidirectional electron transport, we first analyzed the idealized device geometry depicted in Figure 3a. This scenario assumes the maximum possible asymmetry of absorption with only one of the gold nanoelectrodes illuminated. The calculation of the steady-state energy distribution of the subpopulation of hot electrons accounts for the time dependence of both electron−electron (∼100 fs) and electron−phonon (∼1 ps) scattering. Intuitively, optically induced photothermal heating of the entire electron gas occurs after the nonthermal hot electrons are

excited and then thermalized.[13−15] Therefore, if all hot electrons are collected via tunneling before relaxation, we would expect no photothermal heating of the metal. However, we anticipate that both mechanisms of electron excitation (thermal and nonthermal) would be present in the steady state for a real device because of imperfect collection of all nonthermal electrons before they relax. The resulting asymmetric steady-state temperature profile is expected to have a complex dependence on the incident optical power, the thermal conductivity of the materials, and other heat transfer channels present in the system, in addition to the hot carrier collection efficiency. For simplicity, our calculation analyzes the same temperature gradients studied above (ΔT ranges from 0 to 10 K near 300 K), and the nonthermal effect of electron photoexcitation is analyzed as an independent perturbation in

addition to a temperature gradient that results from asymmetric optical absorption. For comparison, we also analyzed the system performance at an elevated temperature (500 to 510 K) corresponding to temperature gradients achieved in solar concentrator schemes.[40]

Figure 3b,e show the $J-V$ profile of Au−vacuum−Au and Au−TiO$_2$−Au plasmonic junctions at two temperature ranges (300 to 310 K and 500 to 510 K) when only one gold nanoelectrode is illuminated by 1000 W/m^2 532 nm monochromatic light. Additionally, we calculated the optical power conversion efficiency by normalizing the maximum output power density by the incident optical power absorbed by the metal. We note that this is a nonideal measure of the device power conversion efficiency, because it does not account for how much optical energy is required to maintain the thermal gradient. As discussed above, greater current density and open-circuit voltage are observed for a Au−TiO$_2$−Au plasmonic junction due to the reduced energy barrier in comparison with an Au−vacuum−Au junction. Near room temperature (300 to 310 K), a significantly increased V_{OC} and J_{SC} is predicted for both a Au−vacuum−Au and a Au−TiO$_2$−Au tunneling junction compared with the purely thermally mediated tunneling discussed in Figure 1. Furthermore, while the range of ΔT is the same, significantly enhanced J_{SC} and V_{OC} are obtained at elevated temperature (500 K) compared to room temperature. Specifically, there is a 100% increase of V_{OC} at 500 K vs 300 K for an Au−vacuum−Au junction (from 220 μV to 440 μV) and a 60% increase of V_{OC} for a Au−TiO$_2$−Au junction (from 400 μV to 640 μV). Figure 3c,f show the power conversion efficiency at different temperatures. In addition, a 3-fold optical power conversion efficiency enhancement from 24% at 300 K to 80% at 500 K is predicted. Thus, electron thermalization interacts cooperatively with nonthermal excitation mechanisms in this device in order to provide larger optical power conversion efficiency.

In order to bolster our hypothesis that asymmetries in electronic excitation across tunneling gaps can be maintained by tailoring the optical response of each metallic nanoelectrode, we used full wave optical simulations (FDTD method, Lumerical Inc.) to simulate the local electric field enhancement and the corresponding photoabsorption in more realistic device geometries. Instead of solving for the potential in these structures, the internal electric field is determined numerically, because the relationship between the position and momentum operators allows for a matrix element that depends on the internal electric field E only,

$$\langle \Psi_f(r)|rE|\Psi_i(r)\rangle = \frac{j\hbar E}{m(\varepsilon_f - \varepsilon_i)}\langle \Psi_f(r)|\hat{p}|\Psi_i(r)\rangle$$

where j is the imaginary unit. The optical power conversion from the devices was then analyzed using the same procedure as for the idealized geometries studied above but with the calculated absorption profiles. The modeled device structures and the corresponding optical absorption spectra are depicted in Figure 4. The spatially integrated spectral absorption by each individual electrode is also displayed in order to emphasize which wavelengths of illumination preferentially excite one electrode more than the other. Since plasmonic nanostructures have significant local electric field enhancement at sharp corners, a tunnel junction consisting of a 20 nm thick triangle-shaped gold nanoelectrode (Au1) was selected that exhibits greater electric field concentration at the sharp tip compared

with the flat edge of a rectangular counter-electrode (Au2) separated by 1 nm. This design is optimized to promote current flow from the region of high absorption in the sharp tip to regions of low absorption in the rectangular counter-electrode.

Several resonant features are observed in the absorption spectra, with a red-shift and more complex broadening observed when the structure is coated with TiO$_2$. Our calculations of the optical power conversion efficiency considered excitation wavelengths that maximized the amount of absorption in one electrode compared to the other, in order to understand the device response under conditions when the electrodes do not absorb light equally. For the Au−vacuum−Au junction these wavelengths are 585 and 785 nm, and for the Au−TiO$_2$−Au junction these wavelengths are 658 and 707 nm, with an incident power of 1000 W/m^2 in all calculations. Figure 4b,f show the local electric field enhancement at these excitation wavelengths in the region centered on the gap. It should be noted that there is no fundamental reason that the calculations cannot be expanded to analyze gold nanoelectrodes with larger size. However, the simulation cost would increase significantly with the increasing physical dimensions, because the matrix elements require calculations between all two-state combinations, and the number of states increases tremendously with the volume of the metal. It should also be noted that even though these incident wavelengths were selected because they are absorbed preferentially by one electrode in the junction, we still observed stronger local electric field concentration at the sharp tip of the triangular electrode regardless of the incident wavelength, as would be preferred for broadband optical power conversion. Indeed, current flows from the triangular electrode to the rectangular electrode for all incident wavelengths simulated.

The optical power conversion efficiency was calculated by normalizing the maximum output power by the incident optical power that was absorbed by the entire structure. While stronger electric field enhancement was calculated when the Au−vacuum−Au junction is illuminated by 785 nm compared to 585 nm monochromatic irradiation, the power conversion efficiency shows little wavelength dependence. The energy barrier to tunneling is large compared with the energy of electrons that absorb either wavelength of light, and hence the probability of tunneling is greater for electrons excited to higher energy states with 585 nm light. The higher tunneling probability compensates for the lower absorption rate compared with excitation at 785 nm. In contrast the power conversion efficiency calculated for the Au−TiO$_2$−Au junction at a wavelength of 658 nm versus 707 nm (Figure 4h) indicates a strong dependence on wavelength. When the Au−TiO$_2$−Au junction is illuminated by 707 nm irradiation, greater efficiency (20.2%) is achieved compared to 658 nm illumination (16.84%). In this device the barrier height of the Au−TiO$_2$−Au junction is reduced to 1 eV, which is smaller than the incident photon energy. Therefore, rather than tunneling, a greater portion of electrons are photoemitted, and the current density more directly indicates the local field enhancement and photoexcitation rate.

■ CONCLUSION

In this study, we have developed a theoretical model that accounts for electron tunneling, photoemission, and thermionic emission across tunneling junctions defined by plasmonic metal nanostructures that absorb light asymmetrically. The roles of photothermal heating and hot carrier excitation are analyzed

separately, and our results indicate that both effects interact cooperatively to promote an electrical current from the electrode with greater local field concentration to the electrode with less field concentration. When only optically induced thermal gradients are considered, electron tunneling dominates transport across the junction near room temperature. Photo-excitation of hot carriers under an optical flux comparable to solar illumination increases the current provided by the device and allows for a theoretical optical power conversion efficiency of up to 80% when the junction is at an elevated temperature of 500 K and subject to a temperature gradient of 10 K. Furthermore, full wave optical simulations of more realistic device geometries show that the directionality of the induced current flow is independent of excitation wavelength across the visible spectrum. Up to 20% power conversion efficiency is achieved in a modeled Au−TiO$_2$−Au device structure under 707 nm monochromatic illumination with an intensity of 1000 W/m^2 when the junction is subject to a thermal gradient of ΔT = 10 K. We believe these results will inform strategies for more efficient device implementation of optical power converters based on plasmonic absorption in metals.

■ AUTHOR INFORMATION

Corresponding Author

*E-mail: sheldonm@tamu.edu.

ORCID

Shengxiang Wu: 0000-0002-1173-5569

Matthew T. Sheldon: 0000-0002-4940-7966

Notes

The authors declare no competing financial interest.

■ ACKNOWLEDGMENTS

■ REFERENCES

(1) Green, M. A.; Hishikawa, Y.; Dunlop, E. D.; Levi, D. H.; Hohl-Ebinger, J.; Ho-Baillie, A. W. Y. Solar cell efficiency tables (version 51). *Prog. Photovoltaics* **2018**, *26* (1), 3−12.

(2) Lewis, N. S. Research opportunities to advance solar energy utilization. *Science* **2016**, *351* (6271), aad1920.

(3) Jain, P. K.; Huang, X.; El-Sayed, I. H.; El-Sayed, M. A. Review of Some Interesting Surface Plasmon Resonance-enhanced Properties of Noble Metal Nanoparticles and Their Applications to Biosystems. *Plasmonics* **2007**, *2* (3), 107−118.

(4) Yang, L.; Pillai, S.; Green, M. A. Can plasmonic Al nanoparticles improve absorption in triple junction solar cells? *Sci. Rep.* **2015**, *5*, 11852.

(5) Zhu, S.-Q.; Zhang, T.; Guo, X.-L.; Shan, F.; Zhang, X.-Y. Light Absorption Enhancement in Organic Solar Cell by Embedding Ag Nanoparticles and Nanochains within the Active Layer. *J. Nanomater.* **2014**, *2014*, 1−8.

(6) Fu, W. F.; Chen, X.; Yang, X.; Wang, L.; Shi, Y.; Shi, M.; Li, H. Y.; Jen, A. K.; Chen, J. W.; Cao, Y.; Chen, H. Z. Optical and electrical effects of plasmonic nanoparticles in high-efficiency hybrid solar cells. *Phys. Chem. Chem. Phys.* **2013**, *15* (40), 17105−11.

(7) Schuller, J. A.; Barnard, E. S.; Cai, W.; Jun, Y. C.; White, J. S.; Brongersma, M. L. Plasmonics for extreme light concentration and manipulation. *Nat. Mater.* **2010**, *9* (3), 193−204.

(8) Gan, Q.; Bartoli, F. J.; Kafafi, Z. H. Plasmonic-enhanced organic photovoltaics: breaking the 10% efficiency barrier. *Adv. Mater.* **2013**, *25* (17), 2385−96.

(9) Lee, J.-Y.; Peumans, P. The origin of enhanced optical absorption in solar cells with metal nanoparticles embedded in the active layer. *Opt. Express* **2010**, *18*, 10078−10087.

(10) Atwater, H. A.; Polman, A. Plasmonics for improved photovoltaic devices. *Nat. Mater.* **2010**, *9* (3), 205−13.

(11) Eustis, S.; El-Sayed, M. A. Why gold nanoparticles are more precious than pretty gold: Noble metal surface plasmon resonance and its enhancement of the radiative and nonradiative properties of nanocrystals of different shapes. *Chem. Soc. Rev.* **2006**, *35*, 9.

(12) Sonnichsen, C.; Franzl, T.; Wilk, T.; von Plessen, G.; Feldmann, J.; Wilson, O.; Mulvaney, P. Drastic reduction of plasmon damping in gold nanorods. *Phys. Rev. Lett.* **2002**, *88* (7), 077402.

(13) Mubeen, S.; Hernandez-Sosa, G.; Moses, D.; Lee, J.; Moskovits, M. Plasmonic photosensitization of a wide band gap semiconductor: converting plasmons to charge carriers. *Nano Lett.* **2011**, *11* (12), 5548−52.

(14) Moslovits, M. Hot Electrons Cross Boundaries. *Science* **2011**, *332*, 2.

(15) Ferry, V. E.; Munday, J. N.; Atwater, H. A. Design considerations for plasmonic photovoltaics. *Adv. Mater.* **2010**, *22* (43), 4794−808.

(16) DuChene, J. S.; Tagliabue, G.; Welch, A. J.; Cheng, W.-H.; Atwater, H. A. Hot Hole Collection and Photoelectrochemical CO$_2$ Reduction with Plasmonic Au/p-GaN Photocathodes. *Nano Lett.* **2018**, *18*, 254510.1021/acs.nanolett.8b00241.

(17) Paul, K. K.; Giri, P. K. Role of Surface Plasmons and Hot Electrons on the Multi-Step Photocatalytic Decay by Defect Enriched Ag@TiO2 Nanorods under Visible Light. *J. Phys. Chem. C* **2017**, *121* (36), 20016−20030.

(18) Chalabi, H.; Schoen, D.; Brongersma, M. L. Hot-Electron Photodetection with a Plasmonic Nanostripe Antenna. *Nano Lett.* **2014**, *14* (3), 1374−1380.

(19) Leenheer, A. J.; Narang, P.; Lewis, N. S.; Atwater, H. A. Solar energy conversion via hot electron internal photoemission in metallic nanostructures: Efficiency estimates. *J. Appl. Phys.* **2014**, *115* (13), 134301.

(20) Chen, H.; Su, L.; Jiang, M.; Fang, X. Highly Desirable Photodetectors Derived from Versatile Plasmonic Nanostructures. *Adv. Funct. Mater.* **2017**, *27* (45), 1704181.

(21) Govorov, A. O.; Zhang, H. Kinetic Density Functional Theory for Plasmonic Nanostructures: Breaking of the Plasmon Peak in the Quantum Regime and Generation of Hot Electrons. *J. Phys. Chem. C* **2015**, *119* (11), 6181−6194.

(22) Furube, A.; Hashimoto, S. Insight into plasmonic hot-electron transfer and plasmon molecular drive: new dimensions in energy conversion and nanofabrication. *NPG Asia Mater.* **2017**, *9*, e454.

(23) García de Arquer, F. P.; Mihi, A.; Kufer, D.; Konstantatos, G. Photoelectric Energy Conversion of Plasmon-Generated Hot Carriers in Metal−Insulator−Semiconductor Structures. *ACS Nano* **2013**, *7* (4), 3581−3588.

(24) McCarthy, P. T.; Reifenberger, R. G.; Fisher, T. S. Thermionic and Photo-Excited Electron Emission for Energy-Conversion Processes. *Front. Energy Res.* **2014**, *2*, DOI: 10.3389/fenrg.2014.00054.

(25) Inc, L. http://www.lumerical.com/tcad-products/fdtd/.

(26) Fowler, R. H.; S, F. R.; Nordheim, L. Electron emission in intense electric fields. *Proc. R. Soc. London, Ser. A* **1928**, *119* (781), 173−181.

(27) Jensen, K. L. General formulation of thermal, field, and photoinduced electron emission. *J. Appl. Phys.* **2007**, *102* (2), 024911.

(28) Murphy, E. L.; Good, R. H. Thermionic Emission, Field Emission, and the Transition Region. *Phys. Rev.* **1956**, *102* (6), 1464−1473.

(29) Lee, Y. K.; Park, J.; Park, J. Y. The Effect of Dye Molecules and Surface Plasmons in Photon-Induced Hot Electron Flows Detected on Au/TiO2 Nanodiodes. *J. Phys. Chem. C* **2012**, *116* (35), 18591−18596.

(30) Manjavacas, A.; Liu, J. G.; Kulkarni, V.; Nordlander, P. Plasmon-Induced Hot Carriers in Metallic Nanoparticles. *ACS Nano* **2014**, *8* (8), 7630−7638.

(31) Hartland, G. V. Optical Studies of Dynamics in Noble Metal Nanostructures. *Chem. Rev.* **2011**, *111* (6), 3858−3887.

(32) Bodurov, I.; Yovcheva, T.; Sainov, S. Refractive index investigations of nanoparticles dispersed in water. *Journal of Physics. J. Phys.: Conf. Ser.* **2014**, *558* (1), 012062.

(33) Cui, L.; Jeong, W.; Fernández-Hurtado, V.; Feist, J.; García-Vidal, F. J.; Cuevas, J. C.; Meyhofer, E.; Reddy, P. Study of radiative heat transfer in Ångström- and nanometre-sized gaps. *Nat. Commun.* **2017**, *8*, DOI: 10.1038/ncomms14479.

(34) St-Gelais, R.; Zhu, L.; Fan, S.; Lipson, M. Near-field radiative heat transfer between parallel structures in the deep subwavelength regime. *Nat. Nanotechnol.* **2016**, *11*, 515.

(35) Fang, Y.; Jiao, Y.; Xiong, K.; Ogier, R.; Yang, Z.-J.; Gao, S.; Dahlin, A. B.; Käll, M. Plasmon Enhanced Internal Photoemission in Antenna-Spacer-Mirror Based Au/TiO2 Nanostructures. *Nano Lett.* **2015**, *15* (6), 4059−4065.

(36) Zhao, G.; Kozuka, H.; Yoko, T. Sol—gel preparation and photoelectrochemical properties of TiO2 films containing Au and Ag metal particles. *Thin Solid Films* **1996**, *277* (1), 147−154.

(37) Zolotavin, P.; Evans, C. I.; Natelson, D. Substantial local variation of the Seebeck coefficient in gold nanowires. *Nanoscale* **2017**, *9* (26), 9160−9166.

(38) Svensson, R.; Holmlid, L. Very low work function surfaces from condensed excited states: Rydberg matter of cesium. *Surf. Sci.* **1992**, *269−270*, 695−699.

(39) Govorov, A. O.; Zhang, H.; Gun'ko, Y. K. Theory of Photoinjection of Hot Plasmonic Carriers from Metal Nanostructures into Semiconductors and Surface Molecules. *J. Phys. Chem. C* **2013**, *117* (32), 16616−16631.

(40) Chirumamilla, M.; Roberts, A. S.; Ding, F.; Wang, D.; Kristensen, P. K.; Bozhevolnyi, S. I.; Pedersen, K. Multilayer tungsten-alumina-based broadband light absorbers for high-temperature applications. *Opt. Mater. Express* **2016**, *6* (8), 2704−2714.